



# Timing and Single-pulse Study of Pulsar J1909+0122 Discovered by CRAFTS

Yutong Chen<sup>1,2</sup>, Pei Wang<sup>1,3</sup>, Di Li<sup>1,2,4</sup>, Erbil Gügercinoğlu<sup>1</sup>, Rushuang Zhao<sup>1,5</sup>, Lingqi Meng<sup>1,2</sup>, Jianping Yuan<sup>6</sup>, Jiarui Niu<sup>1,2</sup>, Weiwei Zhu<sup>1,3</sup>, Yi Feng<sup>4</sup>, Chenchen Miao<sup>1,2</sup>, Chenhui Niu<sup>1,7</sup>, Qingdong Wu<sup>6</sup>, Na Wang<sup>6</sup>, Shen Wang<sup>8</sup>, Xiaoyao Xie<sup>5</sup>, Mengyao Xue<sup>1</sup>, Jumei Yao<sup>6</sup>, Mao Yuan<sup>1,2</sup>, Shanping You<sup>5</sup>, Xuhong Yu<sup>5</sup>, Youling Yue<sup>1</sup>, Jie Zhang<sup>9</sup>, Junshuo Zhang<sup>1,2</sup>, Lei Zhang<sup>1</sup>, Yabiao Wang<sup>10</sup>, Zhenye Gan<sup>10</sup>, Yuxi Li<sup>10</sup>, Zhongyi Sun<sup>10</sup>, and Chengjie Wang<sup>10</sup>

<sup>1</sup>National Astronomical Observatories, Chinese Academy of Sciences, Beijing 100101, China; [wangpei@nao.cas.cn](mailto:wangpei@nao.cas.cn)

<sup>2</sup>University of Chinese Academy of Sciences, Beijing 100049, China

<sup>3</sup>Institute for Frontiers in Astronomy and Astrophysics, Beijing Normal University, Beijing 102206, China

<sup>4</sup>Research Center for Intelligent Computing Platforms, Zhejiang Laboratory, Hangzhou 311100, China

<sup>5</sup>Guizhou Normal University, Guiyang 550001, China

<sup>6</sup>Xinjiang Astronomical Observatory, Chinese Academy of Sciences, Urumqi 830011, China

<sup>7</sup>College of Physical Science and Technology, Central China Normal University, Wuhan 430079, China

<sup>8</sup>Fudan University, Shanghai 200443, China

<sup>9</sup>Qilu Normal University, Jinan 250200, China

<sup>10</sup>Tencent Youtu Lab, Shanghai 200233, China

Received 2023 March 27; revised 2023 April 13; accepted 2023 April 17; published 2023 July 10

## Abstract

We report the discovery of PSR J1909+0122 by the Five-hundred-meter Aperture Spherical Radio Telescope (FAST) as part of the Commensal Radio Astronomy FAST Survey. PSR J1909+0122 has a spin period of 1.257 s and a dispersion measure of  $186.2 \text{ pc cm}^{-3}$ . The averaged pulse profile shows two distinct components. We performed a single-pulse study based on a one-hour observation at 1.25 GHz on 2021 August 23. We used a threshold of  $5\sigma_{\text{ep}}$  to measure the nulling fraction (NF) as  $63\% \pm 1.5\%$ . The longitude-resolved fluctuation spectra and fast Fourier transform spectra of the binary sequences revealed the quasi-periodicity of nulling with a period of 30 rotation periods. We examined the reliability of the periodicity by comparing it to random noise injection. The NF,  $\dot{E}$ , and modulation periodicity  $P_M$  of PSR J1909+0122 were compared with other periodic nulling pulsars, showing that the source of J1909+0122 has the second largest NF in the population. Long-term timing observations over six months were used to derive the phase-connected ephemeris of this pulsar. The measured  $P$  and  $\dot{P}$  values disfavor dipolar geometry for polar gap models, and the prediction for a space-charge-limited flow model in the case of inverse Compton scattering is only just above the death line. In this work, PSR J1909+0122 has revealed possible correlations between nulling behavior and pulsar properties, which will help to shed light on the pulsar emission mechanism and its temporal evolution in future observations.

*Key words:* (stars:) pulsars: general – (stars:) pulsars: individual (PSR J1909+0122) – stars: neutron

## 1. Introduction

Radio pulsars are known to exhibit multiple emission phenomena such as nulling (Backer 1970b), subpulse drifting (Drake & Craft 1968), and mode changing (Backer 1970a). Pulse nulling is the abrupt disappearance of emission from some pulsars for many rotation periods. The cessation of emission may occur over all frequencies (Ritchings 1976; Wang et al. 2007) and last from one rotation period to months (e.g., PSR B1931+24, Kramer et al. 2006). The fraction of nulling pulses (nulling fraction, NF) could also range from essentially zero to over 90%. The NF is an important parameter for characterizing a nulling pulsar. It has been suggested that the NF is inversely correlated with the age of the pulsar (Ritchings 1976; Wang et al. 2007). But pulsars with similar NFs can have quite different nulling behaviors (Gajjar et al. 2012).

The nulling phenomenon was first discovered by Backer (1970b). There are two classes of models (Konar & Deka 2019) that explain this phenomenon—intrinsic and geometric. The intrinsic causes include, for example, the loss of the coherence conditions (Filippenko & Radhakrishnan 1982), changes in current flow in the magnetosphere (Timokhin 2010), an extreme case of mode changing (Esamdin et al. 2005; Wang et al. 2007; Timokhin 2010; Young et al. 2014), etc. The transition between two states has been considered a random process for decades. Herfindal & Rankin (2007, hereafter HR07) first reported periodicity in the nulling of the bright Cambridge pulsar B1133+16, which had been the object of multiple studies. There were studies of PSR B1133+16 before HR07 (Slee & Mulhall 1970; Taylor & Huguenin 1971; Backer 1973) that had noted a long-period modulation feature. But the periodicity was not revealed until HR07 “washed out”

other factors that could affect the fluctuation spectrum by using an artificial pulse sequence in which they substituted the average profile for the profiles of the active pulses. With the cleaned data, a modulation period of 32 rotation periods was found. HR07 explained both the nulling phenomenon and its periodicity by the geometric effects mentioned above, where the line of sight passing between emitted sub-beams gives rise to “pseudo-nulls”.

More periodic nulling pulsars have been identified after HR07 (Herfindal & Rankin 2009; Rankin & Wright 2008; Basu et al. 2017, 2018, 2020a, 2020b; Basu & Mitra 2019). There are 30 periodic nulling pulsars (Basu et al. 2020b; Wang et al. 2021b) out of over 140 nulling pulsars (Sheikh & MacDonald 2021) found so far. Basu et al. (2020b) made a detailed study of periodic modulation and found that subpulse drifting has a different relationship between the modulation period and spin-down energy loss than other periodic modulations. Meanwhile, many studies indicate that nulling, subpulse drifting, and mode changing may have a certain relationship. For example, Gajjar et al. (2017) found a unique nulling–drifting interaction in PSR J1840-0840, where the pulsar tends to shut down at the end of a drift band and to switch back to an emission phase at the beginning of a new drift band in both components. Wang et al. (2007) found a close relationship between nulling and mode changing, where the transitions between null and active states were associated with transitions between different modes.

The new pulsar J1909+0122 was discovered by the Five-hundred-meter Aperture Spherical Radio Telescope (FAST) during the Commensal Radio Astronomy FAST Survey (CRAFTS<sup>11</sup>) drift-scan mode. It is a relatively slow pulsar with a period of 1.3 s. The dispersion measure (DM) is 186.2 pc cm<sup>-3</sup>. CRAFTS was designed to perform in drift-scan mode and to observe H I and pulsars simultaneously for optimal efficiency (Nan et al. 2011; Li et al. 2018, 2019). To date, CRAFTS has discovered and confirmed 171 new pulsars (Qian et al. 2019; Zhang et al. 2019; Cameron et al. 2020; Pan et al. 2020; Cruces et al. 2021; Wang et al. 2021a, 2021b; Tedila et al. 2022; Wen et al. 2022). The subsequent confirmatory observation, timing, and one-hour tracking observations of PSR J1909+0122 were also performed with FAST.

In this paper we report the discovery and analysis of PSR J1909+0122. In Section 2, we describe the observations and data reduction. Our analysis and results are presented in Section 3 including a single-pulse study and timing residuals. A discussion and a brief summary are given in Sections 4 and 5.

## 2. Observations and Data Reduction

Since FAST is the largest and most sensitive single-dish radio telescope, the CRAFTS pulsar search program performed

with FAST is efficient due to its requirement of a relatively short integration time (Li et al. 2018). PSR J1909+0122 was discovered in 2020 February using the CRAFTS drift-scan mode. It was then confirmed in 2021 July using FAST grid observations to locate its position. After the confirmation, we arranged 22 times of observations from 2021 August 18 to 2022 February 28 including a one-hour observation on 2021 August 23. All the observations were performed for pulsar timing, and the one-hour observation covering 2757 single pulses was used for single-pulse analysis.

The frequency range of all of our observations was 1000–1500 MHz, of which the effective band was 1050–1450 MHz due to the radio-frequency interference (RFI) and low response at the edges. The total number of channels was 4096, except for the observations on 2021 August 24, December 5, and 2022 January 27, which had 1024 channels. The data were recorded in tracking mode using the central beam of the FAST 19 beam receiver (Jiang et al. 2020) with full-Stokes. Each time of observation started with a one-minute or two-minute calibration noise diode, depending on the duration of the observation, for calibration of polarization.

As a newly discovered pulsar, we had no ephemeris to fold the raw data. We processed the data of the confirmatory observation with the pulsar search and analysis software, PRESTO<sup>12</sup> (Ransom 2011). After removing the RFI, we obtained an initial ephemeris with a given spin period ( $P_{\text{obs}}$ ) and a dispersion measure (DM). We then used this ephemeris to fold the data from a one-hour observation on 2021 August 23. We determined a new  $P_{\text{obs}}$  by aligning the peaks of single pulses at the same longitude and a new DM with the best signal-to-noise ratio (S/N). The new ephemeris was used to fold all the observations including the one-hour observation itself.

We folded the raw data using DSPSR<sup>13</sup> (van Straten et al. 2011). The RFI was cleaned by both PAZ and PAZI programs from PSRCHIVE<sup>14</sup> (Hotan et al. 2004). The times of arrival (ToAs) were obtained by PAT.

We used the one-hour observation on 2021 August 23 for the single-pulse analysis. Each spin period was divided into 2048 phase bins while folding. Calibration of polarization was performed using PAC from PSRCHIVE and the Stokes parameter  $I$  is used as intensity.

## 3. Data Analysis and Results

### 3.1. Nulling and Pulse Energy Distributions

Our single-pulse study is based on the one-hour observation covering 2757 spin periods on 2021 August 23. The “pulse stack,” i.e., a sequence of consecutive single pulses, of PSR

<sup>11</sup> <http://crafts.bao.ac.cn/>

<sup>12</sup> <https://github.com/scottransom/presto>

<sup>13</sup> <http://dspsr.sourceforge.net>

<sup>14</sup> <http://psrchive.sourceforge.net>

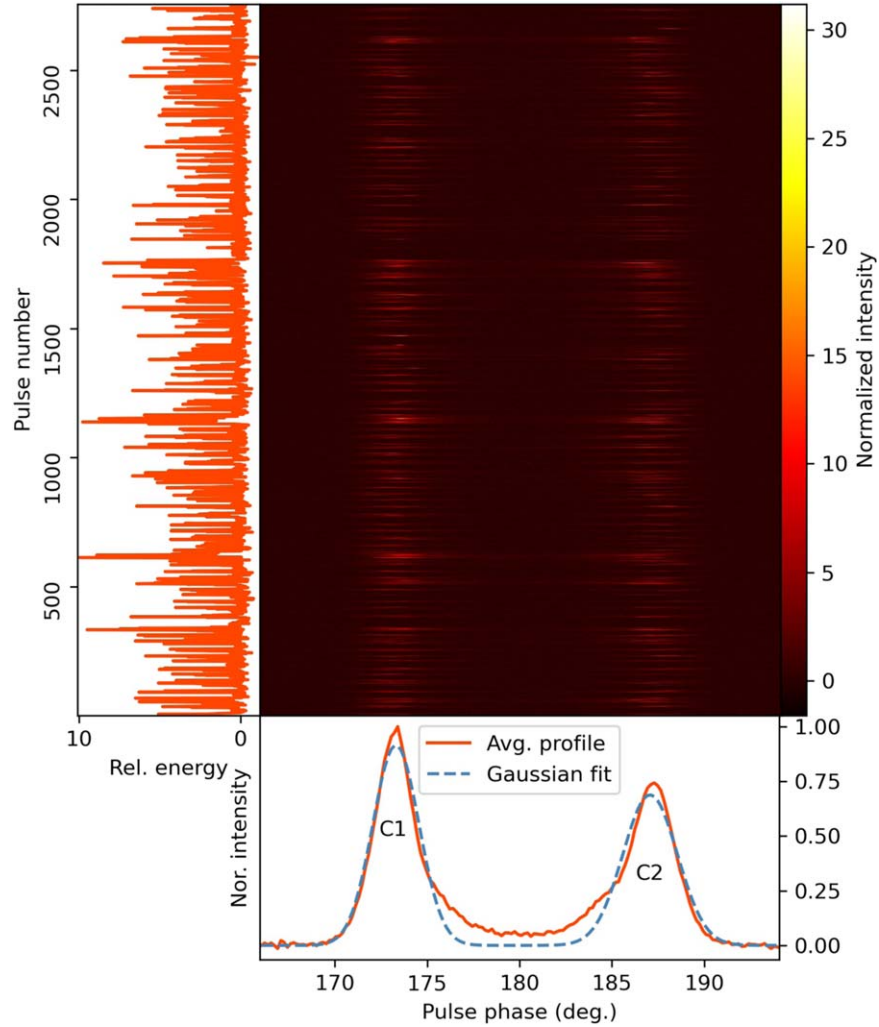


**Figure 1.** The main heat map shows the pulse stack of PSR J1909+0122 with intensity normalized to the peak of the average profile. The lower panel presents the profile averaged over all the pulses (red solid line) and a double-Gaussian fit to it (blue dashed line). The relative energy for each pulse is presented in the left panel.

J1909+0122 is shown in Figure 1, along with the average profile in the lower panel and the relative energy variation in the left panel. The intensity of each period is normalized to the peak of the average profile. The profile has two well-separated components of which the leading one dominates and has higher intensity. Between these two components is a weak bridging region of emission. Along the pulse count axis, the nulling phenomenon is obvious and a quasi-periodicity could be detected by visual inspection. The periodicity is discussed in Section 4.4.

We followed Kramer et al. (1994) to perform a double-Gaussian fit to the average profile. The Gaussian parameters were determined using the least-squares algorithm. The widths of the two components ( $w_{50}$ ), estimated by using the FWHM of the fitting Gaussian function, are  $4^{\circ}.15 \pm 0^{\circ}.10$  and  $4^{\circ}.92 \pm 0^{\circ}.15$

at the central frequency of 1250 MHz, respectively. The leading components have a somewhat sharper shape in most pulses while the trailing components are broader and have a lower flux peak.

The pulse energy distribution has been used to characterize the phenomenon of nulling (Ritchings 1976; Biggs 1992). We examined the energy distributions of the “on-pulse” and “off-pulse” regions and both components. The on-pulse energy is the summed intensity of the on-pulse region extending from  $3\sigma_1$  ( $\sigma_1$  was obtained from the Gaussian fit to the leading component) on the left of the first/leading Gaussian peak to  $3\sigma_2$  on the right of the second/trailing Gaussian peak. The off-pulse window has the same length and is chosen from a region with a relatively stable baseline. The on-pulse and off-pulse energy histograms are shown in the left panel of Figure 2. The

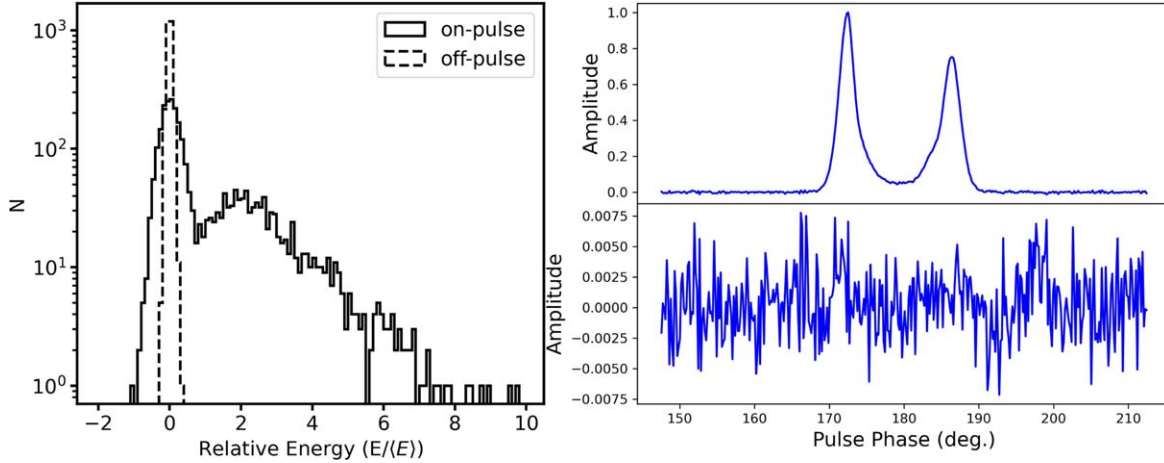


**Figure 2.** (Left) Energy distribution for on-pulse (solid line) and off-pulse (dashed line) regions.  $\langle E \rangle$  is the averaged on-pulse energy. (Right) The burst profile and null profile of PSR J1909+0122. There is no significant emission in the null profile. The amplitudes were normalized to the peak of the active profile.

bimodal distribution shows that the on-pulse energy has a peak at zero, corresponding to null pulses, and another peak at about 2, due to the NF of about 60%.

Before estimating the energy distributions of both components, it is necessary to distinguish nulls from pulse-active or burst states. The histograms above give us only rough information and we need more details to identify individual nulls. We followed Bhattacharyya et al. (2010) and compared the on-pulse energy with a threshold based on the system noise level to identify a null. The uncertainty of the on-pulse energy is given by  $\sigma_{ep} = \sqrt{n_{on}} \sigma_{off}$ , where  $n_{on}$  is the number of on-pulse bins and  $\sigma_{off}$  is the rms of the off-pulse region. Given the high sensitivity of FAST, we chose  $5 \times \sigma_{ep}$  as the threshold. Pulses with on-pulse energy below this threshold were classified as null pulses. This definition was also used to identify null states of both components. We also confirmed that the threshold we used was appropriate by integrating active and null pulses. The profiles are shown in the right panel of Figure 2. There is no emission detected above our threshold within the integrated “null profile.”

According to the null-active sequence created above, the estimated NF is  $63\% \pm 1.5\%$ . The uncertainty of the NF is given by  $\sqrt{n_p}/N$ , where  $n_p$  is the number of nulling pulses and  $N$  is the total number of pulses (Wang et al. 2007).

Single pulses were divided into four states also using the  $5\sigma_{ep}$  threshold, where the on-pulse range was  $3\sigma$  ( $\sigma$  was obtained from the Gaussian fit to the component) left and right of the peak of the component and  $\sigma_{off}$  is the rms of the off-pulse region with the same length as the on-pulse region: active/burst state, null state, and single-component active states. Then we were able to determine the energy distributions for both components. The distributions are shown in Figure 3, where the total number of active pulses is 957 and 834 for the leading and trailing components, respectively. These results show that the

first component has more active pulses and is concentrated in a more energetic region than the second component.

### 3.2. Nulling Behavior

#### 3.2.1. Nulling Profiles and Duration

The transition patterns between two states can indicate the mechanism behind switches. For example, PSR B0818-41 (Bhattacharyya et al. 2010) was reported to have certain transition patterns while switching. The patterns in PSR J1727-2739 (Wen et al. 2016; Rejep et al. 2022) were more complicated, and there were both abrupt and gradual processes in the transitions. For our pulsar we also found different transition patterns, which are shown in Figure 4. This shows that a certain transition process is not always gradual or abrupt.

We integrated the first active pulses (FAP) after null and the last active pulses (LAP) before null to compare with the average profile of all active pulses, since there are pulsars reported to have differences between these profiles (e.g., Deich et al. 1986; Gajjar et al. 2014; Wen et al. 2016; Rejep et al. 2022). The three profiles are shown in Figure 5, all normalized with their own peak intensity. The leading component in all three profiles has a higher peak, and the peaks of the trailing component are 0.75, 0.91, and 0.78 for the all-pulse profile, FAP, and LAP, respectively. So the differences are 0.25, 0.09, and 0.22. As a reference, their baseline rms are 0.003, 0.010, and 0.009. The FAP profile has two more equal components, while the all-pulse and LAP profiles have more similar leading-dominant profiles. The difference between the FAP and LAP profiles may indicate that the magnetosphere of the neutron star is under different conditions during these two processes.

Before further examining the quasi-periodicity indicated by the pulse stack, the distributions of null and burst durations are shown in Figure 6. According to the figure, both short bursts

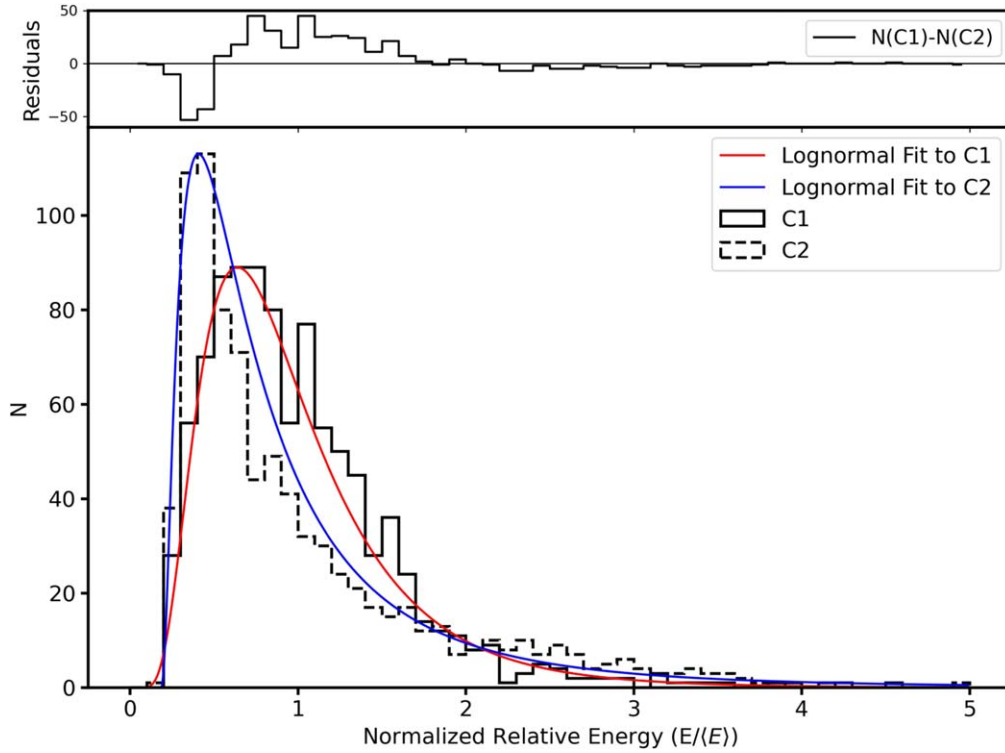


**Figure 3.** Energy distributions of the leading component (C1, solid line) and trailing component (C2, dashed line).  $\langle E \rangle$  is the averaged energy for each component. The residual in the upper panel is the count C2 subtracted from C1. The total numbers of active pulses of the two components are 957 and 834, respectively.

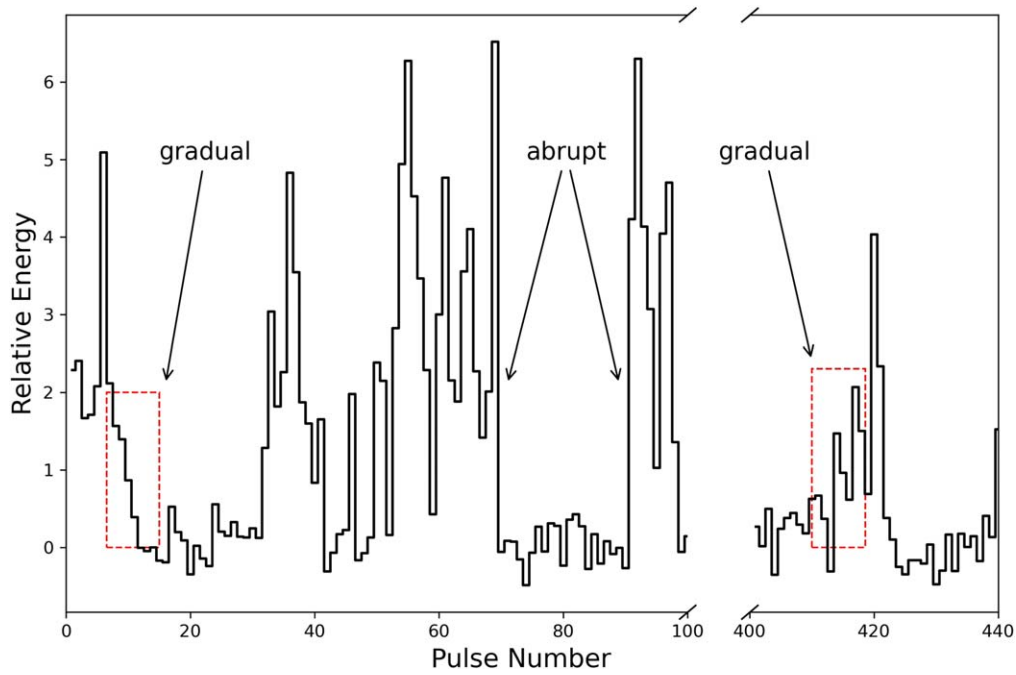


**Figure 4.** Relative energy vs. pulse number from pulses 1 to 100 and 400 to 440. The energy could rise or fall either abruptly or gradually.

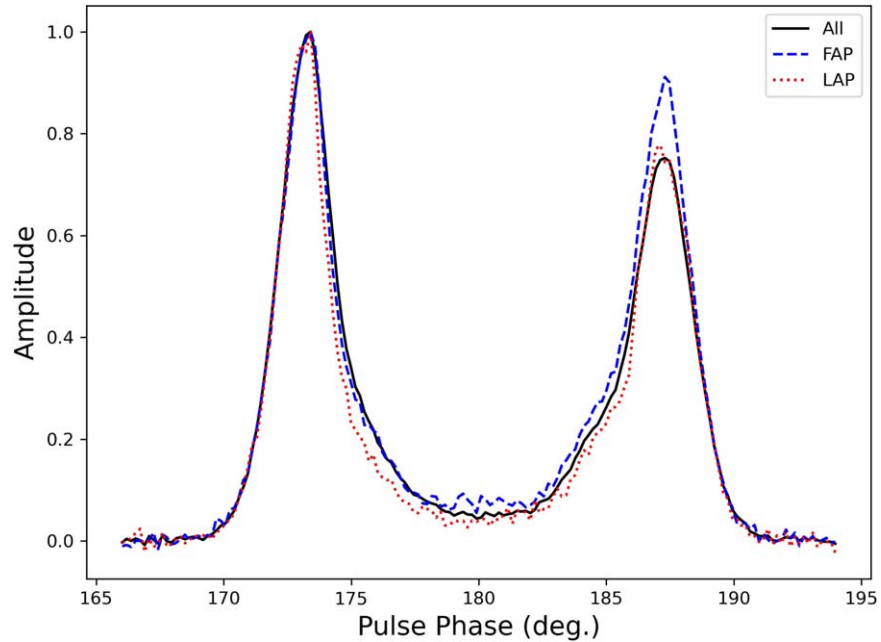


**Figure 5.** Integrated profiles of all active pulses (black solid line), first active pulses (FAP, blue dashed line), and last active pulses (LAP, red dotted line). They were normalized to their own peak intensity.

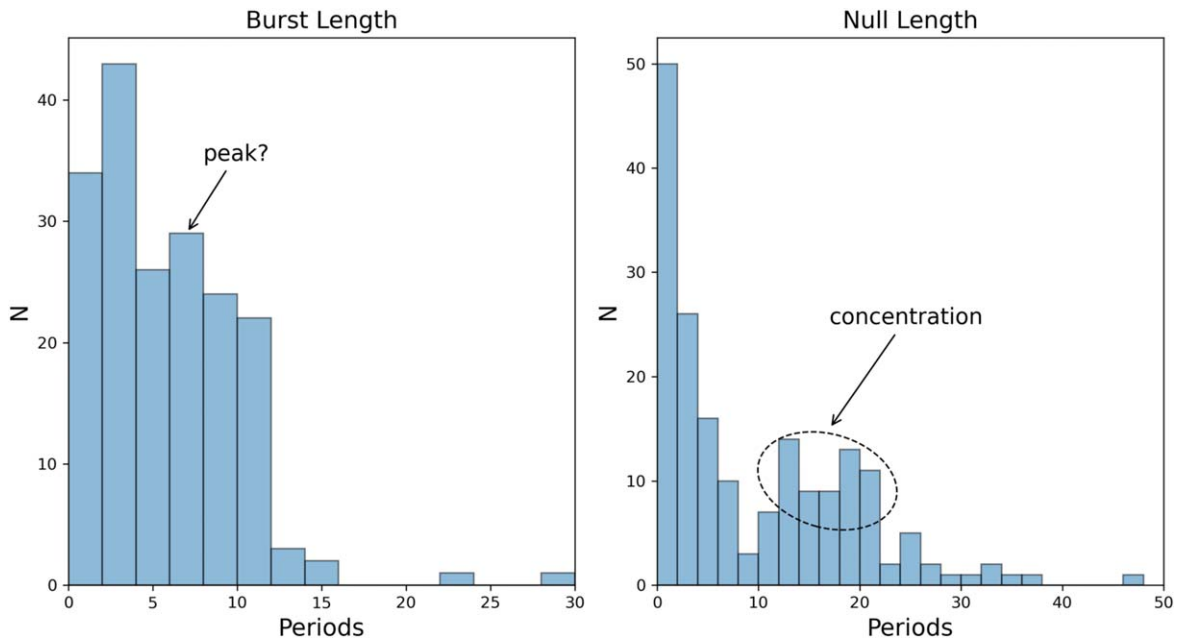


**Figure 6.** Histograms of burst duration (left panel) and null duration (right panel). The suspected peak of the burst duration distribution and the concentration area of null durations are marked.

and nulls are most frequent. But besides the short lengths, there are visible concentrations of both distributions: the burst distribution has a not quite obvious peak around seven periods, and null lengths occur more frequently between 10 and 20

periods. This concentration may be the statistical origin of the periodic modulation of the nulling, while short nulls and bursts may play an important role in leading the periodicity to quasi-periodicity.

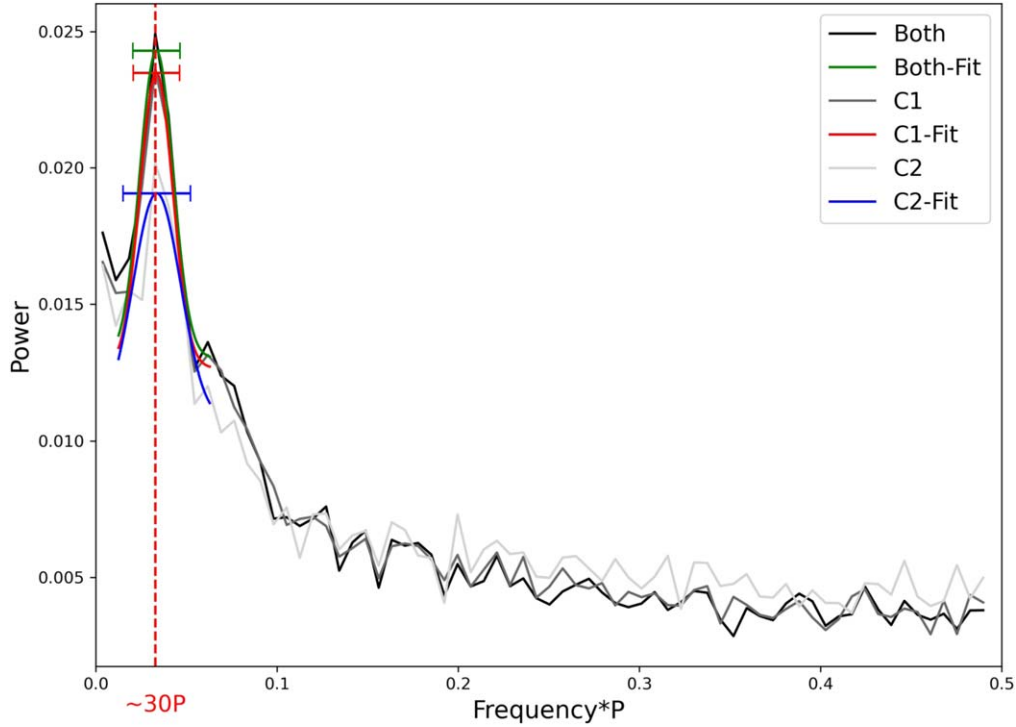


**Figure 7.** Nulling FFT spectrum of PSR J1909+0122, computed using binary sequences generated from pulses in null or active states. The green, red, and blue lines are Gaussian fits of the peaks of both components, C1, and C2, respectively.

### 3.2.2. Quasi-periodic Nulling

We first used the longitude-resolved fluctuation spectra (LRFS, Backer 1973) to estimate the significance of the periodicity. The integrated spectrum showed a peak around 30 rotation periods. However, this peak did not have a high S/N and could only be well distinguished from the noisy background by the smoothed line. Many factors, such as the variation of the pulse amplitude or giant pulses, can be the cause of this “white noise.” Our purpose is to eliminate all other effects and focus only on the nulling behavior itself. Herfindal & Rankin (2007) generated artificial pulse sequences by substituting the average profile for each active pulse to avoid effects caused by profile fluctuations. The integrated spectrum obtained from LRFS subsequently showed a more significant peak and less “white” fluctuation after this processing.

Here we used a more direct method to eliminate the interference. We generated a binary sequence where “0” represented nulls and “1” represented active pulses. This ensured that all subpulse information was washed away and the only possible periodicity was contained in the transitions between the two states (Basu et al. 2017). We also generated similar sequences for both components to confirm that the periodicity of the single component and that of both components were consistent.

We then performed a fast Fourier transform (FFT) on the above binary sequences. The power spectra are shown in Figure 7, where the peak positions are  $30 \pm 11$ ,  $30 \pm 16$ , and  $30 \pm 12$  rotation periods for C1, C2, and both components, respectively. The positions were obtained by Gaussian fitting and the uncertainty was estimated from  $\sigma$  of the fit. These periods are in good agreement with each other and also with the period shown in LRFS as well. First, the same position of the three peaks shows that the periodicity is reliable, and second, the peaks at 30 rotation periods in spectra of binary sequences indicate that the low-frequency feature in LRFS is caused by nulling rather than subpulse drifting.

A Fourier transform was also performed on shorter sequences to examine the time evolution of the periodicity. We used 256 points to compute a spectrum and then shifted the starting point also by 256 points each time. The result is shown in Figure 8. It can be seen that the brighter pixels, which represent the peaks of the spectra, are in a stable region as the starting number increases. Thus, the integrated spectrum in the lower panel therefore shows a peak at about 30 rotation periods, which coincides with the periods given in the LRFS and total nulling FFT spectrum. These aligned peaks imply that the nulling periodicity is time-invariant.

We wondered whether the low-frequency feature in the FFT spectrum was caused by real periodicity, since it was not as

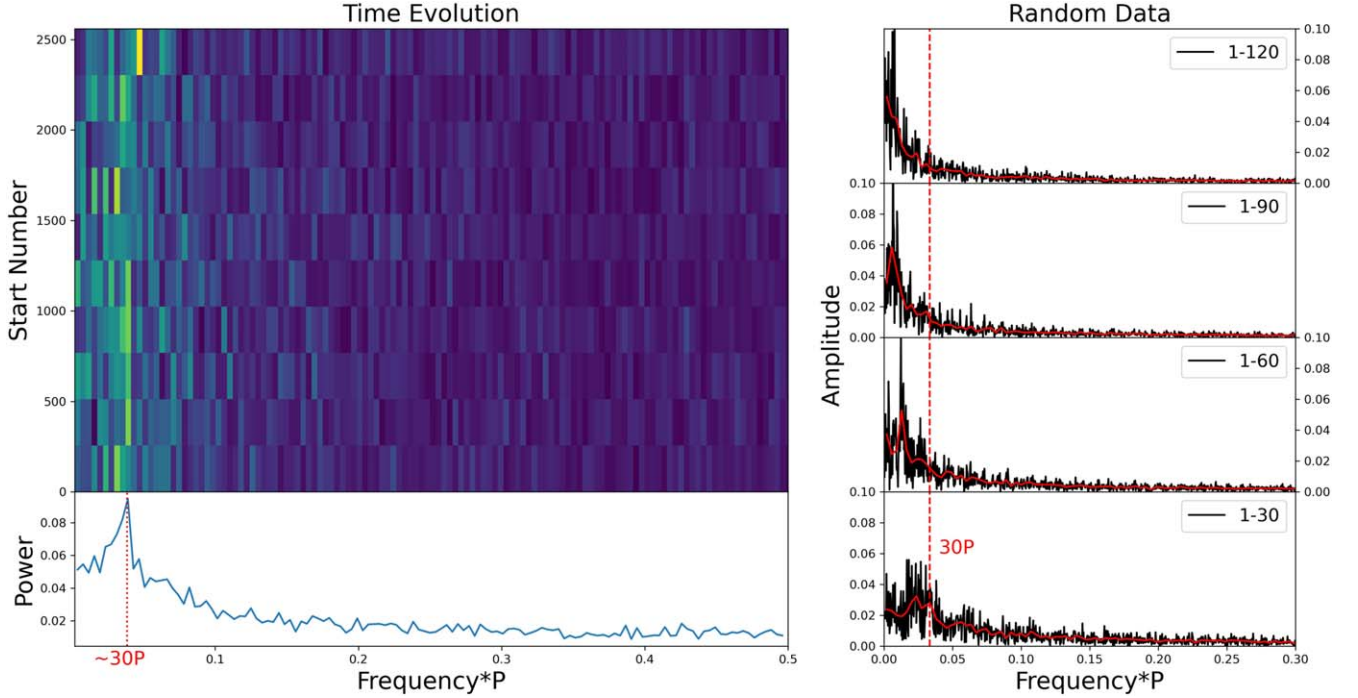


**Figure 8.** (Left) The time evolution of nulling FFT spectra of PSR J1909+0122. The peak of the spectra (upper panel) is at a stable position as the start number increases and leads to the peak in the integrated spectrum (lower left panel). (Right) Spectra computed from random data. The distribution intervals of null or burst duration are displayed in each subfigure.

strictly periodic as, for example, the rotational periodicity of the pulsar itself. Then we constructed test binary sequences that had the same length but randomly distributed nulling and burst duration. FFT was also performed on these sequences to check whether their spectra also had peaks, and the positions of the peaks if they did. Four spectra from our experiment are shown in the right panel of Figure 8. For each spectrum, the duration of the null or burst is evenly and randomly distributed in the interval given in the figure. It can be seen that as the distribution interval shrinks, the spectrum changes from a red-noise-like spectrum to a spectrum with a peak. However, even if the sum of the central values of nulling and burst duration is 30, the peak of the spectrum is not at exactly 30 rotation periods. On the one hand, our quasi-periodic nulling can be distinguished from a random process. On the other hand, if the spectrum of random data requires a relatively concentrated distribution interval to approximate our result, then the random sequence itself could be considered quasi-periodic.

### 3.3. Pulsar Timing Observations

To derive the time solution of PSR J1909+0122, more than six months of long-term timing observations were performed. For both high S/N and full data utilization, we integrated 100 spin periods and cross-correlated the integrated profile with the template for a ToA. The template used was the integrated

profile of our longest observation on 2021 August 23. By visual inspection, we ensured that the profiles integrated over 100 periods were stable. We used the TEMPO2<sup>15</sup> (Hobbs et al. 2006) software to find the timing solution for the ToAs, which extend over 194 days. The timing residuals are shown in the left panel of Figure 9. This is obviously an isolated pulsar and can be modeled well with simple parameters. The timing parameters are given in Table 1. Three derived parameters are also presented: the pulsar’s characteristic age ( $\tau_c = P/2\dot{P}$ ), its surface magnetic field strength ( $B_s = 3.2 \times 10^{19} \sqrt{P\dot{P}}$  G), and its rotational energy loss ( $\dot{E} = 4\pi^2 I \dot{P}/P^3$  where  $I \sim 10^{45}$  g cm<sup>2</sup> is the moment of inertia of the neutron star).

Multicomponent pulsars can provide “single-component-dominant” templates for timing. Feng et al. (2021) divided single pulses into two types by comparing the intensity of their two components. Then they created two templates that had a larger leading component or a larger trailing component. They found that using different templates could not improve the rms residuals for the millisecond pulsar. We followed this process to see whether the same was true for slow pulsars. We averaged single pulses of each type to obtain two single-component-dominant templates for subsequent timing. The single-component timing residuals are shown in the right panel of Figure 9.

<sup>15</sup> <https://bitbucket.org/psrsoft/tempo2>

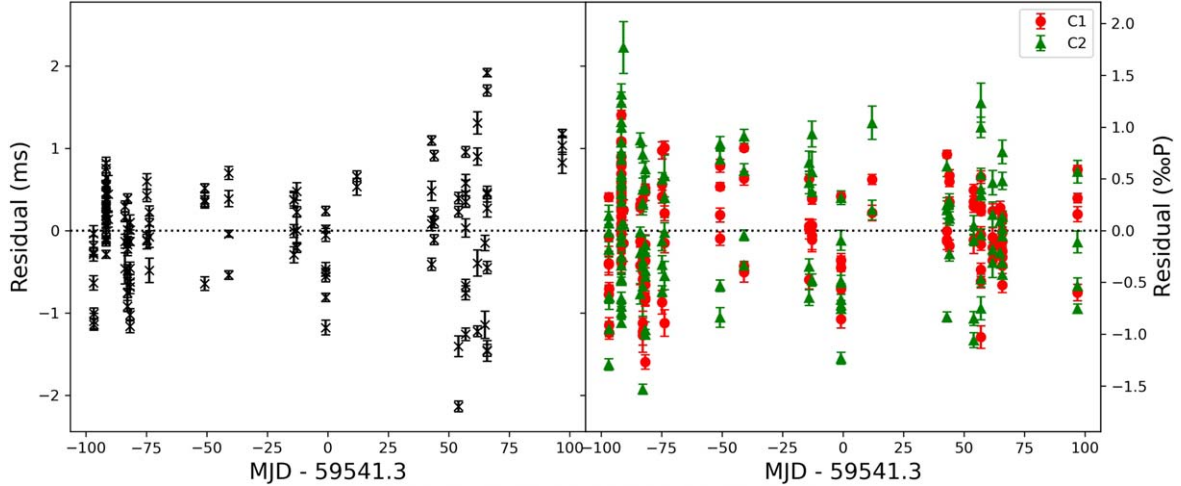


**Figure 9.** Timing residuals corresponding to 22 times of observations extending over 194 days. Residuals in the left panel were obtained by using average profile as a template. Residuals in the right panel were obtained by using C1-dominant (red circles) and C2-dominant (green triangles) templates.

As in Feng et al. (2021), the results were not improved by this method, where the rms of the left panel was 0.655 ms and the rms of the leading component (C1) and the trailing component (C2) were 0.581 ms and 0.764 ms, respectively, which means that timing with only the average profile is sufficient.

### 3.4. Mode Changing and Subpulse Drifting

As mentioned above, the low-frequency feature in the LRFS was proved to be generated by quasi-periodic zeroing. We found no other evidence for the occurrence of subpulse drifting.

To find a possible mode changing, we first assumed that the change was periodic, meaning that both modes had a certain length and repeated in turn. We defined a parameter to look for this, more specifically to look for two stable modes whose average profiles were exactly opposite in terms of the difference between their two component peaks. The difference between two components of an average profile was  $\delta p = (p_1 - p_2)/(p_1 + p_2)$ , where  $p_1$  was the peak intensity of C1 or the leading component and  $p_2$  was the peak intensity of C2. We changed three parameters to calculate  $\delta p$ : the sum of the lengths of two modes  $l_{\text{sum}}$ , the length of one mode  $l_1$ , and the starting period of this mode  $P_{\text{start}}$ . The  $l_{\text{sum}}$  we tried ranged from 10 to 200,  $l_1$  ranged from 2 to  $l_{\text{sum}} - 2$ , and  $P_{\text{start}}$  ranged from 1 to  $l_1$ . Then we calculated the difference between  $\delta p$  of the average profiles of the two modes according to each set of parameters we chose. Unfortunately, we found that when the sum of the lengths of two modes was constant, when the difference between the  $\delta p$  of two modes was maximized, the length of one mode always minimized to two or three rotation periods. This tendency meant that the profile of the longer mode was exactly the average profile of all pulses, and the shorter mode, consisting of several pulses, happened to have an average profile with large  $\delta p$ . But these modes were not stable.

**Table 1**  
Parameters for PSR J1909+0122

Timing model parameters:	
R.A.(J2000) (h:m:s)	19:09:12.1(3)
Decl.(J2000) (d:m:s)	+01:22:52.7(5)
Galactic longitude (deg)	36.19
Galactic latitude (deg)	-3.32
Dispersion measure, DM ( $\text{pc cm}^{-3}$ )	186.2(4)
Pulse period, $P$ (s)	1.2573806447(5)
Period derivative, $\dot{P}$	$6.3(2) \times 10^{-16}$
Epoch of period (MJD)	59,449
Time standard	TT(TAI)
Time units	TCB
Solar-system ephemeris	DE438
Number of ToAs	129
rms timing residual ( $\mu\text{s}$ )	655
Derived parameters:	
Characteristic age (Myr)	31.5
Surface magnetic field strength (G)	$9.03 \times 10^{11}$
Rotational energy loss ( $\text{erg s}^{-1}$ )	$1.25 \times 10^{31}$
Observations:	
Number of observations	22
Date of first observation (MJD)	59,444
Date of last observation (MJD)	59,638
Total time span (day)	194

**Note.** Uncertainties in parentheses refer to the last quoted digit.

As with the subpulse drifting, we found no evidence of mode changing and subpulse drifting above the  $5\sigma$  level.

## 4. Discussion

We performed a one-hour tracking observation on 2021 August 23, and acquired 2757 single pulses for analysis. The

average profile had two components, of which the leading component was dominant. The nulling phenomenon could be easily identified in the pulse stack, and the energy distribution of the on-pulse region further proved it. Due to the high sensitivity of FAST, instead of fitting the histogram of the energy distribution, we determined whether each individual pulse was null by using a threshold of  $5\sigma_{ep}$  to estimate the NF. The estimated NF was  $63\% \pm 1.5\%$ . We also determined the energy distributions of the two components, which did not match.

We integrated the FAP and LAP and compared them to the average profile. The profiles were all leading-component-dominant, while the profile of the FAP had a higher trailing component. The different patterns at the beginning and end of the nulling may indicate that the neutron star was in a different state during these processes.

Quasi-periodic nulling is the key feature of PSR J1909+0122. We first examined the distributions of nulling and burst duration. After statistical analysis of 36 pulsars, Basu et al. (2017) concluded that nulls of short duration (less than five periods) are dominant. The short nulls and bursts are also most common for PSR J1909+0122. But besides the short durations, both nulls and bursts have another clustering interval, which means that the distribution is not random.

The peaks of the LRFS and subsequent FFT spectra of binary sequences confirm the quasi-periodicity seen in the pulse stack. The estimated modulation period is  $(30 \pm 12)P$ . Spectra computed from double and single components suggest that the two differentially energy-distributed components behave similarly in terms of periodicity. The time evolution of the subspectra indicates that the periodicity does not vary with time. We noticed that several likely long-period pulsars (e.g., Wang et al. 2021c; Rejep et al. 2022) were also calculated in this way. The spectra computed from these pulsars were not significant and the periodicity could not be confirmed. Then we wondered how much our result differed from random data. However, the spectra computed from random sequences did not agree with our result.

Basu et al. (2020b) made a detailed study of the periodic modulation of many pulsars, including 29 periodic nulling pulsars. A figure was displayed to show the relationship between the pulsars' spin-down energy loss and the modulation periods. Here we show a similar figure and introduce NF as a new parameter. In Figure 10 the red circle is PSR J1909+0122. On the one hand, PSR J1909+0122 is in the cluster in the  $\dot{E}$  versus  $P_M$  figure, which means that it is a typical periodic nulling pulsar. On the other hand, it has a relatively large NF. We chose, for example, a threshold of 40% to divide the points into two types. The upper left figure shows that pulsars with larger or smaller NF do not have different distributions. Considering that some of the samples were observed with lower sensitivity, which might ignore weak null emission, NF of these samples might decrease if the sensitivity of their

observations is the same as that of PSR J1909+0122. Thus, PSR J1909+0122 is a high-NF example in the population of periodic nulling pulsars.

Sturrock (1971) predicts inefficiency of the generation of secondary plasma inside magnetospheres of long-period pulsars and in turn an increase in the nulling fraction as a pulsar ages. Since the polar cap shrinks with increasing period and age, the electron acceleration region marginally gives rise to pair creation instability. Hence, electron bunches responsible for coherent radio emission assume the form of thin arcs with a different viewing geometry, resulting in complex pulse morphology that differs from that of simple single pulses. In the carousel model of Ruderman & Sutherland (1975) the phenomenon of subpulse drift is attributed to the sparks ejected into the force-free magnetosphere and their circulatory motion with respect to the magnetic axis. The absence of subpulse features in PSR J1909+0122 is in agreement with a low rotational loss of  $\sim 10^{31}$  erg  $s^{-1}$  of this star. In terms of the carousel model nulling is expected to be the dominant behavior in the pulsar radiation pattern after  $P\dot{E}$  (the amount of spin-down energy lost by the pulsar in one rotation period,  $1.57 \times 10^{31}$  erg for PSR J1909+0122) falls below  $\sim 10^{30}$  erg (Wright 2022). The duration of  $\lesssim 30P$  of nulls for PSR J1909+0122 implies either an unsteady inhomogeneous flow of particles into the emission region or a temporary global breakdown of the emission mechanism (Zhang et al. 2007). We estimated the inclination angle  $\alpha$  (the angle between the magnetic moment and rotation axis) of PSR J1909+0122 by fitting its position angle (PA) of linear polarization to the rotating vector model (Radhakrishnan & Cooke 1969). We used the Markov Chain Monte Carlo (MCMC) method based on the Python packages emcee (Foreman-Mackey et al. 2013) and corner (Foreman-Mackey 2016) to obtain the geometrical parameters, which are shown in Figure 11. Both its position on the  $P - \dot{P}$  diagram and the low inferred value of the inclination angle suggest that PSR J1909+0122 evolves toward the so-called death valley, below which a pulsar is no longer energetic enough to generate radio emission (Chen & Ruderman 1993). The measured values  $P = 1.27$  s and  $\dot{P} = 6.3 \times 10^{-16}$   $s s^{-1}$  disfavor dipolar geometry for polar gap models (Ruderman & Sutherland 1975), and the prediction for the space-charge-limited flow model (Arons & Scharlemann 1979) in the case of inverse Compton scattering is only barely above the death line (Zhang et al. 2000). This observation supports the view that magnetic field structure above the polar cap may have multipolar structure or significantly curved geometry. For pulsars with ages greater than a few million years magnetic field evolution assisted by Hall drift distorts the dipolar field geometry and changes the polar cap structure (Geppert et al. 2021). Hall drift along with the period lengthening–aging effect may be the underlying reason for the two-component pulse shape of comparable equivalent widths for PSR J1909+0122. The fact that old nulling pulsars occupy the same region on the

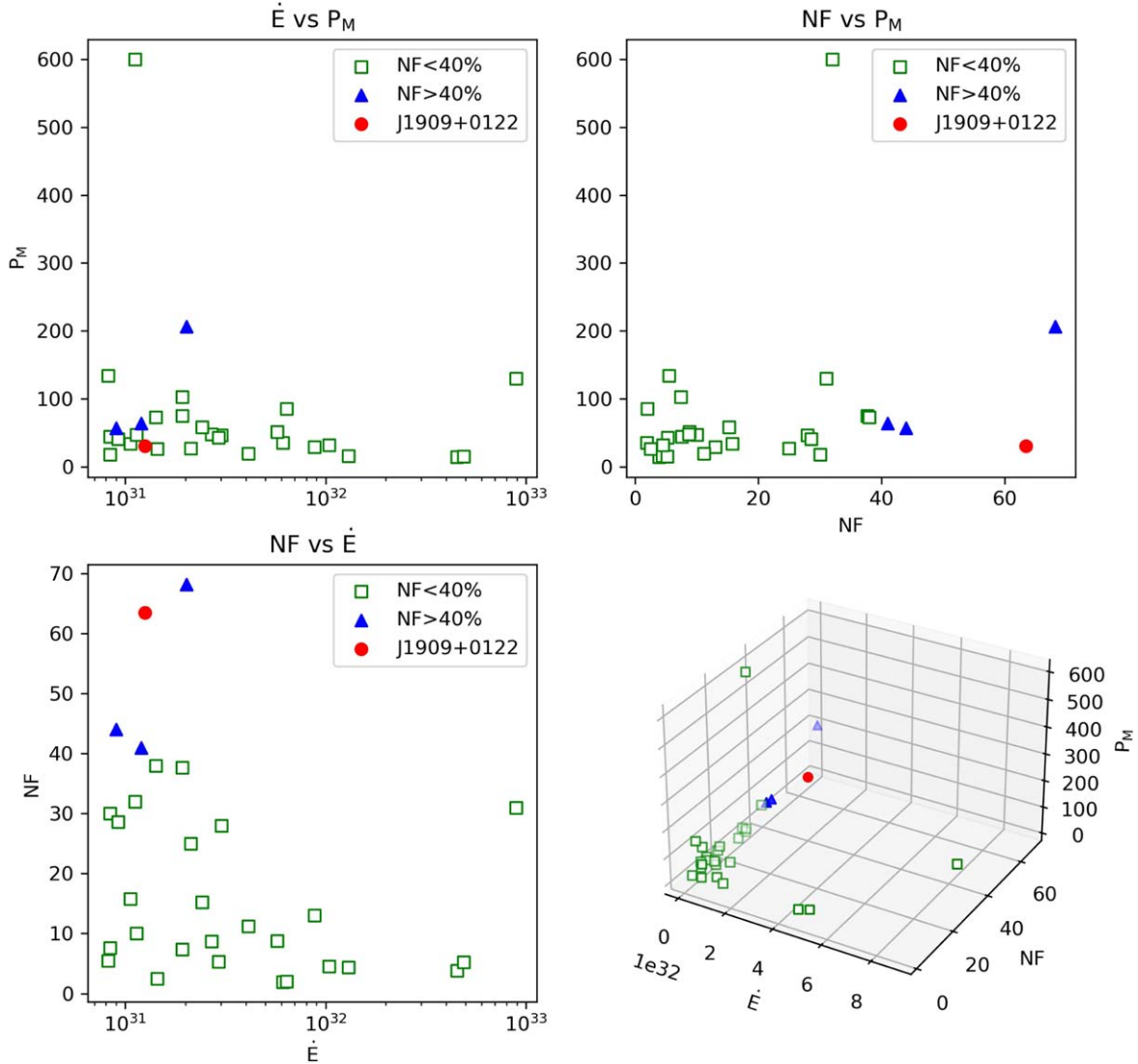


**Figure 10.** Modulation periodicities ( $P_M$ ), nulling fraction (NF), along with rotational energy loss ( $\dot{E}$ ). PSR J1909+0122 is the red circle, plotted along with the high-NF pulsars (blue triangles) and the low-NF pulsars (green squares). It is seen that J1909+0122 has typical  $P_M$  and  $\dot{E}$  but large NF.

$P - \dot{P}$  diagram as rotating radio transients (RRATs) suggests a causal evolutionary connection between them (Philippov & Kramer 2022). RRATs with observed periods in the range 41.5 ms to 7.7 s show a high degree of nulling, exceeding 95% (Abhishek et al. 2022). Pulsars with nulling fractions less than 40% and those above this level constitute two statistically different classes (Konar & Deka 2019; Sheikh & MacDonald 2021). This apparent gap, if it is not a selection effect, may determine whether a long-period nulling pulsar will eventually evolve into an RRAT or not. Future observations of PSR J1909+0122 will reveal possible correlations between nulling behavior and other pulsar properties such as pulse morphology and allow for determination of the pulsar emission mechanism and its evolution with time.

## 5. Summary

In this paper we report a new pulsar, PSR J1909+0122, discovered in the CRAFTS pulsar search program.

- The rotation period of PSR J1909+0122 is 1.257 s. The DM is  $186.2 \text{ pc cm}^{-3}$ .
- We discovered the quasi-periodicity of the nulling phenomenon of J1909+0122 with a period of 30 rotation periods.
- We derived the phase-connected ephemeris of PSR J1909+0122 with rms of timing residuals = 0.655 ms. Then we compared the rms of the single-component timing ( $\text{RMS}_{C1} = 0.581 \text{ ms}$ ,  $\text{RMS}_{C2} = 0.764 \text{ ms}$ ). The rms for both components was consistent and not improved compared to the average profile.

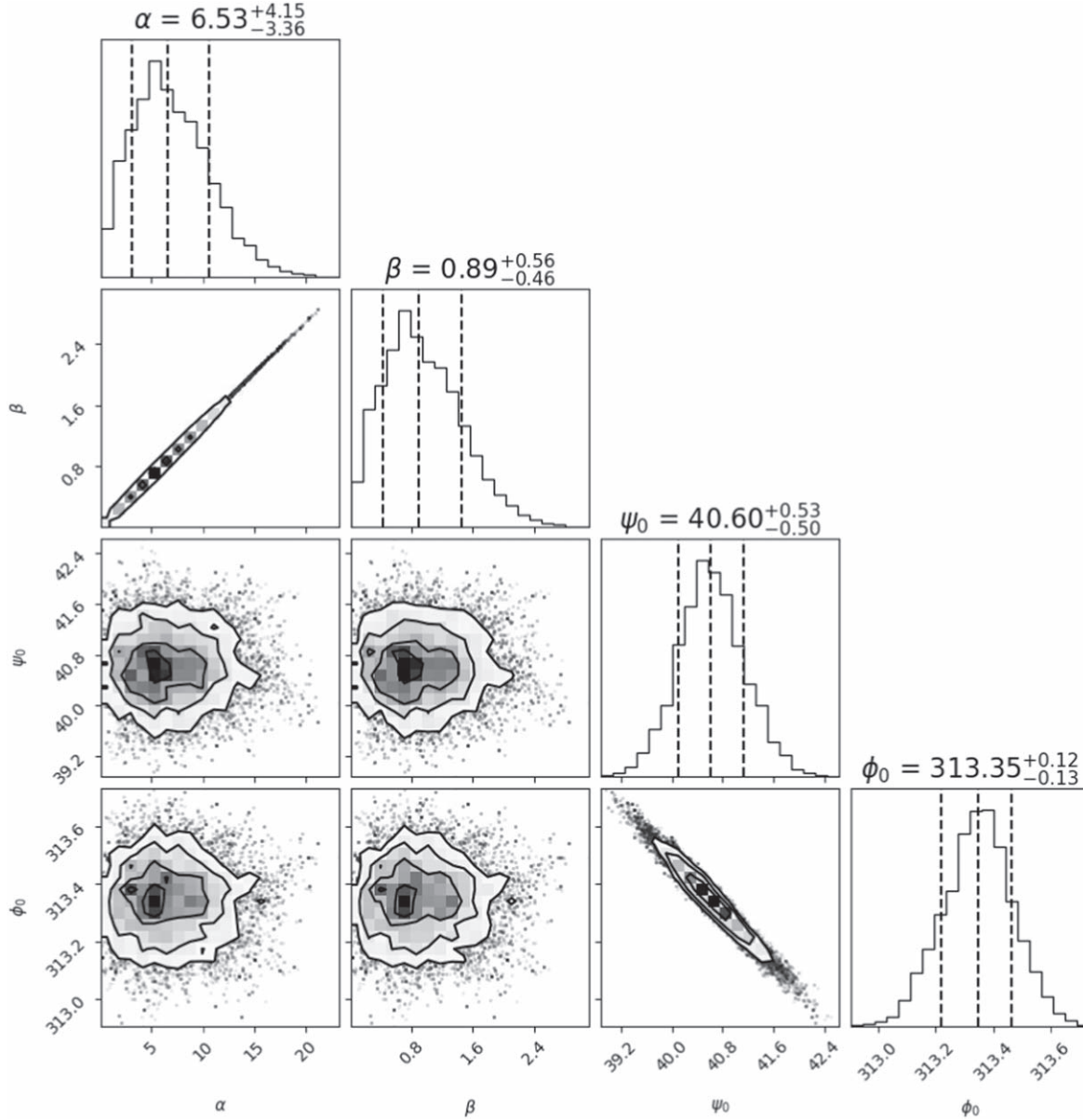


**Figure 11.** Posterior distributions of geometrical parameters  $\alpha$  (magnetic inclination angle),  $\beta$  (angle between the line of sight and the center of the emission beam),  $\Psi_0$  (value of PA when  $\phi = \phi_0$ ), and  $\phi_0$  (pulse phase when PA changes most rapidly) by using the MCMC method. The dashed lines represent 16th, 50th, and 84th percentiles in the corresponding histograms.

- $\dot{P} = 6.3 \times 10^{-16} \text{ s s}^{-1}$  together with the rotation period disfavors the polar gap models and the space-charge-limited flow model. The position of PSR J1909+0122 in the  $P - \dot{P}$  phase diagram demonstrates a possible connection between J1909+0122 and RRATs.

### Acknowledgments

This work has used data from the Five-hundred-meter Aperture Spherical Radio Telescope (FAST). FAST is a

Chinese national mega-science facility, operated by the National Astronomical Observatories of Chinese Academy of Sciences (NAOC). This work is supported by the National Natural Science Foundation of China (NSFC) Grant Nos. 11988101, 11725313, 12041303, 12041304, 12203045, 12203070, 12103013, T2241020, and the National SKA Program of China (Nos. 2020SKA0120200, 2022SKA0130100, 2022SKA0130104), the Foundation of Science and Technology of Guizhou Province (No. (2021) 023), the Foundation of Guizhou Provincial Education

Department (Nos. KY(2021)303, KY(2020)003). P.W. acknowledges support from the National Natural Science Foundation of China under grant U2031117, the Youth Innovation Promotion Association CAS (id. 2021055), CAS Project for Young Scientists in Basic Research (grant YSBR-006) and the Cultivation Project for FAST Scientific Payoff and Research Achievement of CAMS-CAS.

### ORCID iDs

Yutong Chen  <https://orcid.org/0009-0002-9005-694X>  
 Pei Wang  <https://orcid.org/0000-0002-3386-7159>  
 Di Li  <https://orcid.org/0000-0003-3010-7661>  
 Lingqi Meng  <https://orcid.org/0000-0002-2885-568X>  
 Jiarui Niu  <https://orcid.org/0000-0001-8065-4191>  
 Weiwei Zhu  <https://orcid.org/0000-0001-5105-4058>  
 Yi Feng  <https://orcid.org/0000-0002-0475-7479>  
 Chenchen Miao  <https://orcid.org/0000-0002-9441-2190>  
 Chenhui Niu  <https://orcid.org/0000-0001-6651-7799>  
 Shen Wang  <https://orcid.org/0000-0002-1570-7485>  
 Mengyao Xue  <https://orcid.org/0000-0001-8018-1830>  
 Mao Yuan  <https://orcid.org/0000-0003-1874-0800>  
 Youling Yue  <https://orcid.org/0000-0001-6651-7799>  
 Lei Zhang  <https://orcid.org/0000-0001-8539-4237>

### References

- Abhishek, M. N., Tanushree, N., Hegde, G., & Konar, S. 2022, *JapA*, **43**, 75  
 Arons, J., & Scharlemann, E. T. 1979, *ApJ*, **231**, 854  
 Backer, D. C. 1970a, *Natur*, **228**, 1297  
 Backer, D. C. 1970b, *Natur*, **228**, 42  
 Backer, D. C. 1973, *ApJ*, **182**, 245  
 Basu, R., Lewandowski, W., & Kijak, J. 2020a, *MNRAS*, **499**, 906  
 Basu, R., & Mitra, D. 2019, *MNRAS*, **487**, 4536  
 Basu, R., Mitra, D., & Melikidze, G. I. 2017, *ApJ*, **846**, 109  
 Basu, R., Mitra, D., & Melikidze, G. I. 2018, *ApJ*, **857**, 77  
 Basu, R., Mitra, D., & Melikidze, G. I. 2020b, *ApJ*, **889**, 133  
 Bhattacharyya, B., Gupta, Y., & Gil, J. 2010, *MNRAS*, **408**, 407  
 Biggs, J. D. 1992, *ApJ*, **394**, 574  
 Cameron, A. D., Li, D., Hobbs, G., et al. 2020, *MNRAS*, **495**, 3515  
 Chen, K., & Ruderman, M. 1993, *ApJ*, **402**, 264  
 Cruces, M., Champion, D. J., Li, D., et al. 2021, *MNRAS*, **508**, 300  
 Deich, W. T. S., Cordes, J. M., Hankins, T. H., & Rankin, J. M. 1986, *ApJ*, **300**, 540  
 Drake, F. D., & Craft, H. D. 1968, *Natur*, **220**, 231  
 Esamdin, A., Lyne, A. G., Graham-Smith, F., et al. 2005, *MNRAS*, **356**, 59  
 Feng, Y., Hobbs, G., Li, D., et al. 2021, *ApJ*, **908**, 105  
 Filippenko, A. V., & Radhakrishnan, V. 1982, *ApJ*, **263**, 828  
 Foreman-Mackey, D. 2016, *JOSS*, **1**, 24  
 Foreman-Mackey, D., Hogg, D. W., Lang, D., & Goodman, J. 2013, *PASP*, **125**, 306  
 Gajjar, V., Joshi, B. C., & Kramer, M. 2012, *MNRAS*, **424**, 1197  
 Gajjar, V., Joshi, B. C., Kramer, M., Karuppusamy, R., & Smits, R. 2014, *ApJ*, **797**, 18  
 Gajjar, V., Yuan, J. P., Yuen, R., et al. 2017, *ApJ*, **850**, 173  
 Geppert, U., Basu, R., Mitra, D., Melikidze, G. I., & Szkudlarek, M. 2021, *MNRAS*, **504**, 5741  
 Herfindal, J. L., & Rankin, J. M. 2007, *MNRAS*, **380**, 430  
 Herfindal, J. L., & Rankin, J. M. 2009, *MNRAS*, **393**, 1391  
 Hobbs, G. B., Edwards, R. T., & Manchester, R. N. 2006, *MNRAS*, **369**, 655  
 Hotan, A. W., van Straten, W., & Manchester, R. N. 2004, *PASA*, **21**, 302  
 Jiang, P., Tang, N.-Y., Hou, L.-G., et al. 2020, *RAA*, **20**, 064  
 Konar, S., & Deka, U. 2019, *JapA*, **40**, 42  
 Kramer, M., Lyne, A. G., O'Brien, J. T., Jordan, C. A., & Lorimer, D. R. 2006, *Sci*, **312**, 549  
 Kramer, M., Wielebinski, R., Jessner, A., Gil, J. A., & Seiradakis, J. H. 1994, *A&AS*, **107**, 515  
 Li, D., Dickey, J. M., & Liu, S. 2019, *RAA*, **19**, 016  
 Li, D., Wang, P., Qian, L., et al. 2018, *IMMAG*, **19**, 112  
 Nan, R., Li, D., Jin, C., et al. 2011, *IJMPD*, **20**, 989  
 Pan, Z., Ransom, S. M., Lorimer, D. R., et al. 2020, *ApJL*, **892**, L6  
 Philippov, A., & Kramer, M. 2022, *ARA&A*, **60**, 495  
 Qian, L., Pan, Z., Li, D., et al. 2019, *SCPMA*, **62**, 959508  
 Radhakrishnan, V., & Cooke, D. 1969, *ApL*, **3**, 225  
 Rankin, J. M., & Wright, G. A. E. 2008, *MNRAS*, **385**, 1923  
 Ransom, S. 2011, PRESTO: Pulsar Exploration and Search Toolkit, Astrophysics Source Code Library, ascl:1107.017  
 Rejep, R., Wang, N., Yan, W. M., & Wen, Z. G. 2022, *MNRAS*, **509**, 2507  
 Ritchings, R. T. 1976, *MNRAS*, **176**, 249  
 Ruderman, M. A., & Sutherland, P. G. 1975, *ApJ*, **196**, 51  
 Sheikh, S. Z., & MacDonald, M. G. 2021, *MNRAS*, **502**, 4669  
 Slee, O. B., & Mulhall, P. S. 1970, *PASA*, **1**, 322  
 Sturrock, P. A. 1971, *ApJ*, **164**, 529  
 Taylor, J. H., & Huguenin, G. R. 1971, *ApJ*, **167**, 273  
 Tedila, H. M., Yuen, R., Wang, N., et al. 2022, *ApJ*, **929**, 171  
 Timokhin, A. N. 2010, *MNRAS*, **408**, L41  
 van Straten, W., Demorest, P., Khoo, J., et al. 2011, PSRCHEIVE: Development Library for the Analysis of Pulsar Astronomical Data, Astrophysics Source Code Library, ascl:1105.014  
 Wang, N., Manchester, R. N., & Johnston, S. 2007, *MNRAS*, **377**, 1383  
 Wang, P., Li, D., Clark, C. J., et al. 2021a, *SCPMA*, **64**, 129562  
 Wang, S., Zhu, W.-W., Li, D., et al. 2021b, *RAA*, **21**, 251  
 Wang, Z., Wen, Z. G., Yuan, J. P., et al. 2021c, *ApJ*, **923**, 259  
 Wen, Z. G., Wang, N., Yuan, J. P., et al. 2016, *A&A*, **592**, A127  
 Wen, Z. G., Yuan, J. P., Wang, N., et al. 2022, *ApJ*, **929**, 71  
 Wright, G. 2022, *MNRAS*, **514**, 4046  
 Young, N. J., Weltevrede, P., Stappers, B. W., Lyne, A. G., & Kramer, M. 2014, *MNRAS*, **442**, 2519  
 Zhang, B., Gil, J., & Dyks, J. 2007, *MNRAS*, **374**, 1103  
 Zhang, B., Harding, A. K., & Muslimov, A. G. 2000, *ApJL*, **531**, L135  
 Zhang, L., Li, D., Hobbs, G., et al. 2019, *ApJ*, **877**, 55